Acta Crystallographica Section D
Biological Crystallography
ISSN 1399-0047

Low-dose X-ray radiation induces structural alterations in proteins

Valentin Borshchevskiy,[a,b,c,d,e] Ekaterina Round,[a,b,c,d] Ivan Erofeev,[e]‡ Martin Weik,[a,b,c,f] Andrii Ishchenko,[d]§ Ivan Gushchin,[a,b,c,e] Alexey Mishin,[g] Dieter Willbold,[h,d] Georg Büldt[e,i] and Valentin Gordeliy[a,b,c,d,e]*

[a]Université Grenoble Alpes, IBS, 38044 Grenoble, France, [b]CNRS, IBS, 38044 Grenoble, France, [c]CEA, IBS, 38044 Grenoble, France, [d]Institute of Complex Systems (ICS), ICS-6: Structural Biochemistry, Research Centre Jülich, 52425 Jülich, Germany, [e]Laboratory for Advanced Studies of Membrane Proteins, Moscow Institute of Physics and Technology, Dolgoprudniy 141700, Russian Federation, [f]European Synchrotron Radiation Facility, 38027 Grenoble, France, [g]Laboratory for Structural Biology of GPCRs, Moscow Institute of Physics and Technology, Dolgoprudniy 141700, Russian Federation, [h]Institut für Physikalische Biologie, Heinrich-Heine-Universität, Universitätsstrasse 1, 40225 Düsseldorf, Germany, and [i]Institute of Complex Systems (ICS), ICS-5: Molecular Biophysics, Research Center Jülich, 52425 Jülich, Germany

‡ Current address: Laboratory 'Nanostructuring of Membrane-Protein Complexes for the Control of Cell Physiology', Moscow Institute of Physics and Technology, Dolgoprudniy 141700, Russian Federation.
§ Current address: Department of Integrative Structural and Computational Biology, The Scripps Research Institute, CA 92037, USA.

Correspondence e-mail: valentin.gordeliy@ibs.fr

Received 13 December 2013
Accepted 26 July 2014

PDB references: bacteriorhodopsin, 4md1; 4md2

X-ray-radiation-induced alterations to protein structures are still a severe problem in macromolecular crystallography. One way to avoid the influence of radiation damage is to reduce the X-ray dose absorbed by the crystal during data collection. However, here it is demonstrated using the example of the membrane protein bacteriorhodopsin (bR) that even a low dose of less than 0.06 MGy may induce structural alterations in proteins. This dose is about 500 times smaller than the experimental dose limit which should ideally not be exceeded per data set (*i.e.* 30 MGy) and 20 times smaller than previously detected specific radiation damage at the bR active site. To date, it is the lowest dose at which radiation modification of a protein structure has been described. Complementary use was made of high-resolution X-ray crystallography and online microspectrophotometry to quantitatively study low-dose X-ray-induced changes. It is shown that structural changes of the protein correlate with the spectroscopically observed formation of the so-called bR orange species. Evidence is provided for structural modifications taking place at the protein active site that should be taken into account in crystallographic studies which aim to elucidate the molecular mechanisms of bR function.

1. Introduction

It is currently generally accepted that radiation damage to protein crystals is the major challenge in obtaining high-resolution crystallographic protein structures (Garman & Weik, 2013). Synchrotron-radiation facilities (SRF) opened up a new era in structural biology. However, it was accepted from the very beginning of the field that the damage caused by high-intensity ionizing radiation may limit many of the potential biological applications of SRF. The further development of macromolecular cryo-crystallography (Garman, 1999) reduced radiation damage remarkably by cooling crystals to 100 K (Gonzalez & Nave, 1994). Based on electron-microscopy observations, a theoretical dose limit of 20 MGy was proposed, above which significant radiation damage manifested by the degradation of the diffraction properties of macromolecular crystals was predicted to occur (Henderson, 1990). This dose limit was measured experimentally and it was recommended that a dose of 30 MGy should not be exceeded to allow correct biological interpretation of protein structures (Owen *et al.*, 2006). However, specific radiation damage to protein molecules in a crystal occurs at much lower absorbed X-ray doses (for reviews, see Holton, 2009; Garman, 2010). We have recently shown that the first structural signs of specific radiation damage of a membrane protein, bacteriorhodopsin (bR), can be detected in difference Fourier electron-density maps at an absorbed dose of 1.2 MGy (Borshchevskiy *et al.*,

2011), which is 25 times smaller than the experimental dose limit of 30 MGy mentioned above (Owen *et al.*, 2006).

bR is a membrane protein from *Halobacterium salinarum*. The protein harvests energy from light to create an electrochemical gradient across a cell membrane (for a review, see Lanyi, 2004*a*). bR has been one of the most extensively studied membrane proteins during the past 40 years. The Protein Data Bank currently holds 84 published structures of native and mutated bR in the ground and intermediate states (Wickstrand *et al.*, 2014). However, these attempts have failed to propose a complete picture for the molecular mechanism of proton transport (Lanyi, 2004*b*; Hirai *et al.*, 2009) consistent with infrared spectroscopy, which has significantly contributed to our understanding of proton transport across bR (Heberle, 2000; Freier *et al.*, 2011). It has been suggested that specific radiation damage may account for the disagreements between the structures of the earlier intermediates and the corresponding molecular mechanisms of proton pumping published by different research groups (Borshchevskiy *et al.*, 2011).

Specific radiation damage to the bR structure was detected at doses of ∼1.2 MGy by Borshchevskiy *et al.* (2011). However, as described by Matsui *et al.* (2002), changes in the visual absorption spectrum of a bR crystal can be observed at an absorbed dose ∼25 times smaller than that at which specific radiation damage becomes noticeable. It was shown that when a bR crystal at 100 K was exposed to X-ray radiation, nearly half of protein molecules in the ground state was converted into an orange species exhibiting absorption peaks at 450, 478 and 510 nm. Similarly, the M- and possibly L-states were converted to a blue species with an absorption maximum at 650 nm (Takeda *et al.*, 2004; Yamamoto *et al.*, 2009). The fraction of the orange species remained unchanged during further X-ray illumination and it appeared that an equilibrium state between the orange species and the original ground state was established when the cooled crystal was exposed to the X-ray beam. As mentioned in Matsui *et al.* (2002), such an equilibrium may be explained if the ground state is repopulated when the orange species absorbs X-rays. Another possibility is that the protein molecules in the cooled crystal are heterogeneous and only molecules with special conformations are liable to be converted to the orange species. It was noted in Matsui *et al.* (2002) that specific radiation damage of the bR structure and the formation of the orange species take place under significantly different absorbed doses (an ∼25-fold difference) and represents two independent processes.

It is well known that the spectroscopic properties of bR are strongly coupled to the isomerization of retinal and structural rearrangements of the surrounding amino acids and water molecules. Thus, the formation of new (orange or blue) bR species may be coupled to some structural changes that have not been identified before and may be assigned to low-dose radiation damage. Unfortunately, the orange and blue bR species are formed after an absorbed X-ray dose 1–2 orders of magnitude lower than the dose that is usually inflicted during the collection of X-ray crystallographic data. Consequently, the structural nature of the new spectroscopic species has remained elusive.

Here, we present a crystallographic and complementary spectroscopic study of the radiation-induced orange species. We used high-quality $P6_3$ nontwinned bR crystals grown *in meso*, which diffracted to 1.7 Å resolution when a low X-ray dose (∼0.03 MGy) was used to collect a complete data set. We uncover the structural alterations that accompany the spectroscopically detected formation of the orange species that allow us both to determine its structure and to refine the existing model of the bR ground state. The availability of highly ordered bR crystals on the one hand and the possibility of performing independent spectroscopic monitoring of radiation damage on the other open up a unique opportunity to further our current knowledge of X-ray radiation damage to protein structures. This study shows for the first time that the absorption of an X-ray dose lower than 0.06 MGy induces structural alterations in proteins maintained at 100 K during data collection.

2. Materials and methods

2.1. Protein crystallization

The expression and purification of bR has been described in detail by Gordeliy *et al.* (2003). bR crystals were grown in a lipidic cubic phase of monoolein. In accordance with the described procedure, crystallization trials were set up in PCR tubes containing 15 µl of a mesophase of monoolein and bR in CYMAL-5 (5-cyclohexyl-1-pentyl-β-D-maltoside) detergent (Affimetrix). A mixture of dry salts [Na_2HPO_4 (5%) and KH_2PO_4 (95%)] was used as a precipitant. Crystallization probes were incubated at 22°C for 1–2 months. Flat hexagonally shaped plates of 250–600 µm along the plane and 10–70 µm in thickness were obtained. To separate crystals from the lipidic mesophase, 3 *M* sodium phosphate buffer pH 5.6 with 0.1% *n*-octyl-β-D-glucopyranoside was used (Schobert *et al.*, 2002).

2.2. Data collection and processing

Most of the $P6_3$ bR crystals are usually almost perfectly twinned. For these cases, difference Fourier electron-density maps between experimental structure factors of different data sets cannot be calculated. We grew bR crystals in the presence of CYMAL-5 and searched for crystallization conditions giving slow crystal growth (>1.5 months) to increase the number of nontwinned crystals, as has been described previously (Borshchevskiy *et al.*, 2010). The crystals were loop-mounted and flash-cooled on the goniometer in a stream of gaseous nitrogen at 100 K. No additional cryoprotectant was used. Crystals with a low twinning ratio were selected by collecting three to five preliminary diffraction images from each of the crystals on an in-house X-ray generator.

Integration and scaling were performed in *MOSFLM* (Leslie & Powell, 2007) and *SCALA* (Evans, 2006). The twinning ratio was determined using Yeates statistics (http://nihserver.mbi.ucla.edu/Twinning/) and the *DETWIN* routine of *CCP*4 (Yeates, 1997; Winn *et al.*, 2011) as described previously (Borshchevskiy *et al.*, 2010). Two crystals with no

Table 1
Crystallographic statistics of the data used for the study of the bR orange species.

X-ray data were obtained from two crystals of bR at ID14-EH1 (ESRF, Grenoble). Values in parentheses are for the outer resolution shell.

Data set	1	2	3	4	5	6	7	8	9
Crystal 1									
Space group	$P6_3$								
Resolution (Å)	23.44–1.73 (1.82–1.73)								
Twinning ratio (%)	0								
Unit-cell parameters									
$a = b$ (Å)	60.91	60.91	60.91	60.92	60.91	60.92	60.91	60.91	60.93
c (Å)	110.09	110.09	110.09	110.09	110.09	110.11	110.11	110.10	10.15
No. of reflections	59924 (8594)	60023 (8613)	59915 (8592)	59965 (8634)	60237 (8669)	60087 (8634)	60021 (8609)	59869 (8587)	60073 (8638)
No. of unique reflections	22537 (3333)	22550 (3336)	22519 (3324)	22558 (3344)	22568 (3343)	22560 (3336)	22541 (3329)	22526 (3327)	22579 (3341)
Mosaicity (°)	0.59	0.58	0.59	0.59	0.58	0.58	0.58	0.58	0.59
Completeness (%)	93.9 (95.3)	93.9 (95.4)	93.8 (95.0)	93.9 (95.4)	94.0 (95.6)	93.9(95.4)	93.9 (95.2)	93.8 (95.1)	93.9 (95.3)
Wilson B factor (Å^2)	20.2	20.2	20.4	20.2	20.2	20.3	20.4	20.2	21.1
$\langle I/\sigma(I)\rangle$	12.7 (2.7)	12.9 (2.7)	13.1 (2.6)	12.7 (2.5)	12.4 (2.7)	13.1 (2.5)	12.1 (2.6)	12.4 (2.7)	12.0 (2.2)
$R_{\rm merge}(I)$ (%)	4.9 (34.2)	5.0 (33.9)	5.0 (35.3)	5.2 (35.3)	5.1 (35.3)	5.1 (35.4)	5.2 (35.8)	5.2 (36.0)	5.4 (42.8)
$R_{\rm p.i.m.}(I)$ %	3.4 (25.5)	3.6 (25.3)	3.6 (26.2)	3.7 (26.2)	3.6 (26.1)	3.6 (26.3)	3.7 (26.4)	3.7 (26.8)	3.8 (31.7)
Crystal 2									
Space group	$P6_3$								
Resolution (Å)	23.78–1.78 (1.88–1.78)								
Twinning ratio (%)	0								
Unit-cell parameters									
$a = b$ (Å)	60.95	60.95	60.95	60.95	60.95	60.95	60.95		
c (Å)	109.54	109.53	109.55	109.53	109.53	109.53	109.53		
No. of reflections	64422 (9442)	64138 (9393)	64271 (9408)	64273 (9427)	64433 (9414)	64375 (9409)	61716 (9045)		
No. of unique reflections	20756 (3138)	20745 (3135)	20758 (3132)	20749 (3136)	20768 (3138)	20765 (3138)	20522 (3115)		
Mosaicity (°)	0.48	0.48	0.48	0.48	0.48	0.48	0.48		
Completeness (%)	94.2 (96.8)	94.1 (96.8)	94.2 (96.9)	94.2 (96.8)	94.2 (96.9)	94.2 (96.9)	93.1 (96.2)		
Wilson B factor (Å^2)	20.4	20.5	20.4	20.5	20.6	20.6	20.5		
$I/\sigma(I)$	17.2 (4.4)	17.1 (4.5)	17.0 (4.3)	16.9 (4.3)	16.8 (4.1)	16.9 (4.2)	16.8 (4.2)		
$R_{\rm merge}(I)$ (%)	5.2 (38.3)	5.2 (38.7)	5.3 (39.9)	5.4 (41.5)	5.4 (41.6)	5.4 (42.0)	5.2 (38.1)		
$R_{\rm p.i.m.}(I)$ (%)	3.3 (25.7)	3.4 (25.9)	3.4 (26.8)	3.4 (27.9)	3.5 (28.0)	3.5 (28.3)	3.5 (26.2)		

twinning defects were selected for experiments at the synchrotron. The crystals were transported to the synchrotron in liquid nitrogen.

X-ray data were collected on beamline ID14-1 at the European Synchrotron Radiation Facility with a flux density of $\sim10^{12}$–10^{13} photons mm^{-2} s^{-1} at a wavelength of 0.933 Å with no beam attenuation. The crystals were hexagonal plates with dimensions of $\sim400 \times 400 \times 20$ µm. All data were collected at 100 K. Two X-ray images separated by 90° were collected with 0.5 s exposure time and 0.5° oscillation per image. The crystal parameters were determined in *MOSFLM* (Leslie & Powell, 2007). The data-collection strategy was calculated using *BEST* (Bourenkov & Popov, 2006) and data were collected over a total rotation range of ∼40° around the mean crystal rotational orientation, with the small crystal axis parallel to the X axis (if Z is the beam axis and Y is the rotation axis). The dose absorbed by the crystal during pre-screening and alignment can be estimated as several kGy. The size of the beam-defining slits was 160 µm (vertical) and 110 µm (horizontal) so that X-ray data could be collected from three non-overlapping volumes. The X-ray data collection began with the left part of the crystal. 40 images were collected over one third of the total angular range with 0.35° oscillation and 0.54 s exposure per image. Subsequently, the measurement volume was moved to the central and then to the third part of the crystal, where the second and third parts of the total angular range were covered with the same data-collection parameters. As a result, three partial data sets were collected from three non-overlapping crystal regions. The gaps left between the irradiated volumes were ∼20 µm. Partial data sets were merged together later to give a single full data set. Each part of the crystal was exposed to the X-ray beam for 21.6 s. The vertical size of the crystal projection onto the XY plane was smaller than the vertical slits at all rotational positions. The diffracting volume is similar for all three regions and therefore the X-ray doses absorbed by each region are equal. Therefore, the effective exposure time per full data set was 21.6 s. After collection of the third partial data set, the measurement volume was moved to the first part of the crystal and the entire procedure was repeated. Eight full data sets in total were collected in such a manner. After collection of the eighth data set, each part of the crystal was exposed to the X-ray beam with the same experimental parameters but with 25 times the exposure time (13.5 s per image). In the light of our previous experience, the exposure time was chosen to provide a significant (∼1 Å^2) increase in the Wilson B factor, which was used later for the calculation of the dose absorbed by the crystal (§2.3). A ninth data set was then collected in an identical way to the previous eight data sets. Each group of three partial data sets were integrated in *MOSFLM* (Leslie & Powell, 2007) and scaled in *SCALA* (Evans, 2006). As a result, nine data sets with a resolution of 1.73 Å were obtained from the crystal. The same data-collection and reduction procedure was repeated for a second crystal, which was used to show the reproducibility of the results. Data were collected from three crystal volumes with the slits set to 160 mm (vertical) ×

Table 2
Refinement statistics of bR models built for the first and eighth data sets collected from the first crystal.

Values in parentheses are for the outer resolution shell.

Data set	1	8
Resolution (Å)	23.44–1.73 (1.81–1.73)	23.44–1.73 (1.81–1.73)
R (%)	13.9 (15.3)	14.6 (19.2)
$R_{\rm free}$ (%)	18.8 (20.8)	19.0 (22.1)
No. of atoms		
Protein	1786	1823
Lipids	169	169
Water	50	51
R.m.s.d.		
Protein bond lengths (Å)	0.012	0.014
Protein bond angles (°)	1.6	1.7
B factors (Å^2)		
Protein	17.5	17.4
Lipids	45.5	45.5
Water	32.7	32.2

110 µm (horizontal). 46 images were collected from each part with an oscillation of 0.35° and an exposure time of 0.57 s per image. For the second crystal, seven data sets were collected one after another. The resolution of each data set was 1.78 Å. The statistics for each data collection are presented in Table 1.

2.3. Estimation of the absorbed dose

Unfortunately, the X-ray flux at the sample position was not available at the time of the experiment and therefore *RADDOSE-3D* (Zeldin *et al.*, 2013) could not be used to calculate the dose absorbed by the crystal. We therefore used the intrinsic Wilson B-factor increase of a bR crystal exposed to X-ray radiation (Kmetko *et al.*, 2006) as a proxy to estimate the absorbed dose, as described in more detail in Borshchevskiy *et al.* (2011).

The radiation dose absorbed by the crystal for the collection of one data set is small and the B factor did not detectably increase for data sets 1–8 for the first crystal, as well as for data sets 1–7 for the second crystal (Table 1). The crystal was exposed to the X-ray beam for 540 s between the collection of the eighth and ninth data sets as described in §2.2. As a result, the Wilson B factor increased by 0.9 Å^2 between the first and ninth data sets, with a total exposure time between data sets of 712.8 s. Taking into account that the rate of B-factor increase was measured to be 0.9 Å^2 MGy^{-1} (Borshchevskiy *et al.*, 2011), the crystal absorbed 1 MGy between the first and the ninth data sets. We thus estimate that the first crystal absorbed ∼0.030 MGy during the collection of one data set. Similarly, the second crystal absorbed ∼0.037 MGy during one data set. The origin of the errors in this dose estimation in our approach is the uncertainty in the determination of the increase in the B factor, which could be assessed from the data presented in Fig. 6 of Borshchevskiy *et al.* (2011) as the root-mean-square deviation of the ΔB factor calculated for eight consecutive data sets (shown as triangles) from a linear fit. The ΔB-factor error is 0.2 Å^2 and the error in the dose absorbed per single data set is 0.007 and 0.008 MGy for the first and the second crystal, respectively.

To validate our estimations of the absorbed dose per data set, we used an independent approach which exploits the fact that the occupancies of the Asp85 carboxyl group and water molecules in the active site (W401, W402 and W406) decrease linearly with the dose absorbed by the crystal (Fig. 3; Borshchevskiy *et al.*, 2011). The same atoms lost their occupancy by the ninth data set, as can be seen from the difference Fourier electron density ($|F_9| - |F_1|$) map (Fig. 2*h*). The refinement of the mean occupancy of the Asp85 carboxyl group and water molecules W401 and W406 gives 90 ± 4% for the ninth data set, where the error is estimated as a root-mean-square deviation of the occupancies of the individual atoms. The occupancy of W402 was not used in the calculation since it is not only associated with radiolysis of the active site but is also involved in the formation of the orange species, as shown in Figs. 2(*b*)–2(*g*). Therefore, 10% of the protein molecules had a modified active site after the crystal was exposed to the X-ray beam for 712.8 s (between the first and ninth data sets). We calculated previously (Borshchevskiy *et al.*, 2011) that the rate of X-ray modification of the bR active site is 0.12–0.15 MGy^{-1} (see the legend of Fig. 3 in Borshchevskiy *et al.*, 2011). Therefore, one can calculate that the crystal absorbed 0.67–0.83 MGy between the first and ninth data sets, and thus it can be estimated that the first crystal absorbed about 0.020–0.025 MGy for the collection of one data set. Similarly, the second crystal accumulated 0.025–0.032 MGy for the collection of one data set. These estimations agree within the errors with the calculation based on the intrinsic B-factor increase.

2.4. Model building, experimental Fourier difference electron-density maps and structure refinement

The model of the bR ground state was built using the structure factors F_1 from the first data set. The bR ground-state model with PDB code 1c3w (Luecke *et al.*, 1999) was converted to a polyalanine model. Rigid-body refinement and automated macromolecular model building with subsequent refinement was performed in *ARP/wARP* (Perrakis *et al.*, 1999), *REFMAC*5 (Murshudov *et al.*, 2011), *PHENIX* (Adams *et al.*, 2010) and *Coot* (Emsley & Cowtan, 2004). The characteristics of the resulting ground-state model are presented in Table 2 for the first crystal.

Experimental difference Fourier Q-weighted (Bourgeois, 1999) electron-density ($|F_i| - |F_1|$) maps with $i = 2, \ldots, 8$ for the first crystal and $i = 2, \ldots, 7$ for the second crystal were calculated in *CNS* (Brünger *et al.*, 1998) with phases from the ground-state model described above. Figs. 1–3 were prepared in *CHIMERA* (Pettersen *et al.*, 2004)

It follows from the difference electron-density maps that the structural changes accompanying the formation of the orange species are minor and affect only a few molecular groups (Lys216 with the covalently bounded retinal, Met209 and water molecule W402) close to the active site of the protein. For these groups alternative conformations were added at the positions in accordance with the difference maps. The refinement of atom positions in alternative conformations as well as the atom occupancies of both (main and alternative)

conformations was carried out in *PHENIX* against the eighth data set. The refinement statistics of the protein model built against the eighth data set are presented at Table 2.

2.5. Fraction of the bR orange species determined from structural data

The fraction of bR in the orange species was estimated as the mean occupancies of W402, the N atom of the Schiff base (SB) and the S^D atom of Met209 in the corresponding structural model. Occupancies were refined for every data set in a series using *PHENIX* (Adams *et al.*, 2010). As a result, the occupancy of the orange species as a function of the absorbed X-ray dose was obtained (Fig. 5).

2.6. Online microspectrophotometry

Formation of the orange species was traced by monitoring spectral changes in the UV–Vis range using a microspectrophotometer installed on ID14-1 (ESRF, Grenoble; McGeehan *et al.*, 2009). The microspectrophotometer allowed us to obtain crystal spectra in the range 420–900 nm with a spectral resolution of 0.5 nm and a temporal resolution of 0.9 s simultaneously with X-ray exposure. The focal spot of the spectrophotometer at the crystal position was 50 µm in diameter.

Unfortunately, the crystals suitable for X-ray data collection were optically too dense for the collection of UV–Vis spectra. Thus, simultaneous X-ray and UV–Vis spectra data collection could not be carried out. For the spectroscopic studies, crystals of ∼10 µm thickness were selected. The crystal in a cryoloop was flash-cooled to 100 K while it was mounted onto the goniometer. The focus of the microspectrophotometer was adjusted to coincide with the crystal region illuminated by the X-ray beam. The X-ray beam slit size was 170 × 170 µm. The spectroscopic studies were performed on the same day with no beam attenuation, as used during the X-ray data collection. The formation of the orange species was induced by X-ray irradiation and spectroscopic data were collected during irradiation at a fixed crystal orientation. The illumination of the crystal by the spectrophotometer reference beam resulted in the formation of the K-state (Balashov & Ebrey, 2001). The crystal was continuously illuminated with a He–Ne laser (632.8 nm, 17 mW, HRR170, Thorlabs Inc., USA; the $1/e^2$ beam width is 0.98 mm, with the $1/e^2$ beam width corresponding to 1.699 FWHM of a Gaussian beam) when the spectroscopic information was collected to force the K-state back to the ground state as suggested by Balashov & Ebrey (2001).

Aside from the formation of low-temperature intermediate states, we observed a growing peak (400–600 nm) during X-ray exposure. This peak was thought to be associated with the irradiated buffer (it seems likely that the 400–600 nm peak originates from solvated electrons; McGeehan *et al.*, 2009) and this was confirmed by repeating the experiment with the buffer (3 *M* potassium/sodium phosphate pH 5.6) alone. The change in buffer spectrum after irradiation could also be seen by eye as it changed from transparent to a purple colour. In the region of interest the irradiated buffer spectra could be represented by a Gaussian function. The mean value and standard deviation found in the experiment with pure buffer were used in the analysis of the spectra from the bR crystal.

The spectra recorded from the bR crystal were analyzed for the ground state [linear fitting with skewed Gaussian (Metzler & Harris, 1978), peak at 570 nm and buffer spectra found previously] and the time dependence of the peak absorbance $A_{570}(t)$ was extracted. To obtain the kinetics associated with the orange species, the spectra near the 516 nm peak were fitted with a Gaussian on a linear background ($a\lambda + b + A^*_{516}\exp[-\alpha(\lambda - 516)^2]$. Thus, $A^*_{516}(t)$ (but not the total absorbance at a given wavelength) corresponds to the contribution of the orange species. To convert the absorption units to protein quantity the extinction coefficient was required, and while the extinction coefficient for the ground state is known, that for the orange species was not. The orange species relaxes to the ground state under red laser illumination after switching the X-rays off (the A^*_{516} decreases while the A_{570} increases). This observation was used to determine the relative extinction coefficient of the orange species $\beta = \varepsilon^{gr}_{570}/\varepsilon^{or}_{516}$, where ε^{gr}_{570} and ε^{or}_{516} are the extinction coefficients of the ground state and the orange species at 570 and 516 nm, respectively. Assuming that the orange species can de-excite only to the ground state, the decrease in A^*_{516} can be associated with the increase in A_{570}. Consequently, the extinction coefficient, $\beta = 2.0 \pm 0.2$, can be calculated. Using this β value, the amount of orange species formed in the course of the experiment can be calculated from the spectroscopic data (Fig. 5).

The dose absorbed by the crystal per second is almost independent of the depth in the crystal (Murray *et al.*, 2005). This fact allowed the dose absorbed by the thin crystal used for microspectrophotometry to be calculated since the increase in the *B* factor cannot be used to calibrate the dose owing to the low diffraction quality of the crystal. The crystal absorbed 1.4 ± 0.3 kGy s^{-1}.

2.7. PDB accession codes

Coordinates and structure factors have been deposited in the Protein Data Bank with accession codes 4md2 (bR ground state) and 4md1 (bR ground state and orange species).

3. Results

As discussed in Matsui *et al.* (2002), exposure of bR crystals to a relatively low X-ray dose corresponding to only several images (while 110 images comprised a full data set) at cryogenic temperatures results in spectroscopic changes and the formation of the so-called orange species of the protein characterized by absorption peaks at 510, 478 and 450 nm. The formation of the orange species follows a limited exponential growth law $[A_0 - A_1\exp(-t/t_0)]$ with t_0 equal to 251 s. This time is significantly shorter than that required for X-ray dataset collection (2200 s) with the crystals of *P*622 symmetry used in Matsui *et al.* (2002). No structural changes accompanying

the formation of the orange species have been identified in the crystals with *P*622 symmetry (Matsui *et al.*, 2002).

Most of the currently available bR X-ray structures were collected from crystals of $P6_3$ symmetry, with the highest resolution being 1.47 Å (PDB ID 1m0k, 1m0m; Schobert *et al.*, 2002). However, no structural peculiarities which can be interpreted as originating from the formation of the orange species have previously been reported, even for the well diffracting $P6_3$ crystals. One can assume that the structure of the orange species differs only slightly from that of the ground state, so that the differences could not be resolved before with the available structural data.

In the present work, nontwinned large crystals (∼400 × 400 × 20 µm) grown using the *in meso* approach were used. With such crystals, high-resolution (∼1.7 Å) X-ray data sets could be collected with low absorbed doses (∼0.03 MGy per data set). In order to reduce the absorbed dose, complete data sets were collected from three different regions of the crystal as described in detail in §2.2.

As was confirmed by the spectroscopic study described later in §3.4, this dose is within the range of a rapid increase in the content of the orange species in the crystal, and several complete data sets can be collected before the level of the orange species reaches its maximum value. A comparison of data sets with significantly different levels of orange species provides information on the structural changes associated with the formation of the orange species.

We have collected eight such consecutive data sets at 1.73 Å resolution from the same crystal according to the procedure described in detail in §2. To check the reproducibility of the results, seven consecutive data sets were collected from a second crystal at 1.78 Å resolution. X-ray data statistics for both crystals are shown in Table 1. Since both crystals showed similar experimental difference Fourier electron-density maps in the course of orange species formation (§3.1), as well as a similar behaviour of crystallographic statistics, only the results from the first crystal will be discussed in the following.

It should be noted that the X-ray dose absorbed by the crystals for data collection is low (the first crystal absorbs 0.03 MGy per data set as described in §§2.2 and 2.3 and 0.24 MGy was absorbed in total after the collection of the eighth data set) and no signs of global radiation damage were detected. As shown in Table 1, all of the global characteristics of crystal diffraction quality [mosaic spread, *B* factor, unit-cell volume as well as $\langle I/\sigma(I)\rangle$, $R_{\rm merge}$ and $R_{\rm p.i.m.}$ (overall and outer shell)] remain almost the same for data sets 1–8. The crystal was exposed to extensive X-ray illumination (total absorbed dose of ∼1 MGy) after the collection of the eighth data set. The ninth data set was then collected in the same way as the previous data sets.

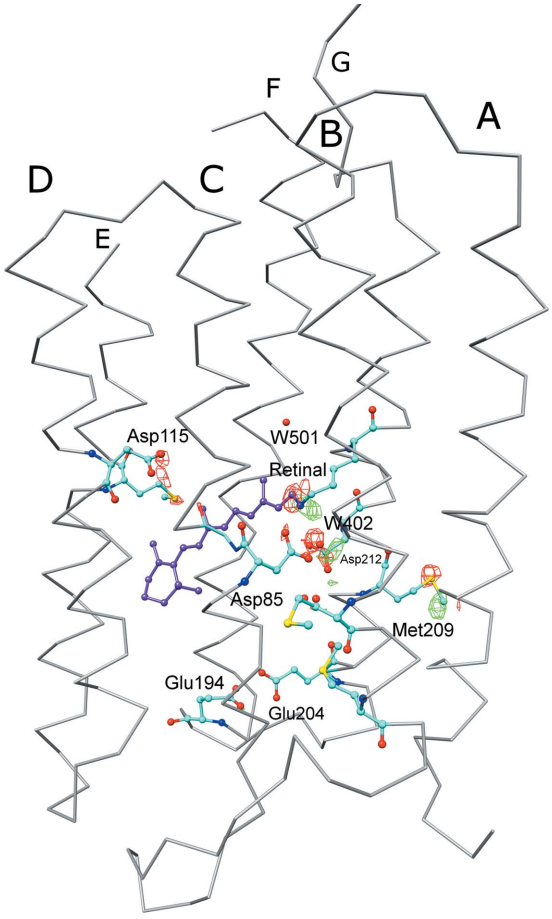

Figure 1
Global view of the experimental Fourier difference electron-density map ($|F_8| - |F_1|$) at 5σ. The negative and positive densities are in red and green, respectively. The molecular groups that are most sensitive to X-ray radiation damage are shown as ball-and-stick models. Retinal is shown in purple.

3.1. Experimental difference Fourier electron-density maps of low-X-ray-dose radiation damage

Experimental difference Fourier electron-density ($|F_i| - |F_1|$) maps were calculated to identify structural changes between subsequent data sets. A global presentation of the protein structural model between the eighth and the first data sets is shown as an ($|F_8| - |F_1|$) map in Fig. 1. At the 3.5σ level, difference electron densities are present at virtually all residues as well as in the solvent region. At the level of 5σ, the difference densities remain only at certain residues and no difference densities are visible in the solvent region. Since the difference densities are randomly distributed in the solvent region at the 3.5σ level, they are assumed to correspond primarily to noise. Difference peaks greater than 5σ were considered as being well above the noise level and were used in structural analysis. The difference electron density is concentrated in the central part of the protein surrounding its active site (see Fig. 1).

Detailed views of the active site with difference Fourier maps between the first and all of the subsequent data sets are shown in Fig. 2. Slight difference density is observed in the ($|F_2| - |F_1|$) map near the water molecule W402 at the bR active site (see Fig. 2*a*). Starting from the ($|F_3| - |F_1|$) map, difference densities appear near the SB and the side chain of Met209, which is located ∼10 Å away from the active site. These difference densities increase substantially in the ($|F_i| - |F_1|$) maps with i = 3, 4, 5 and 6; however, the difference maps

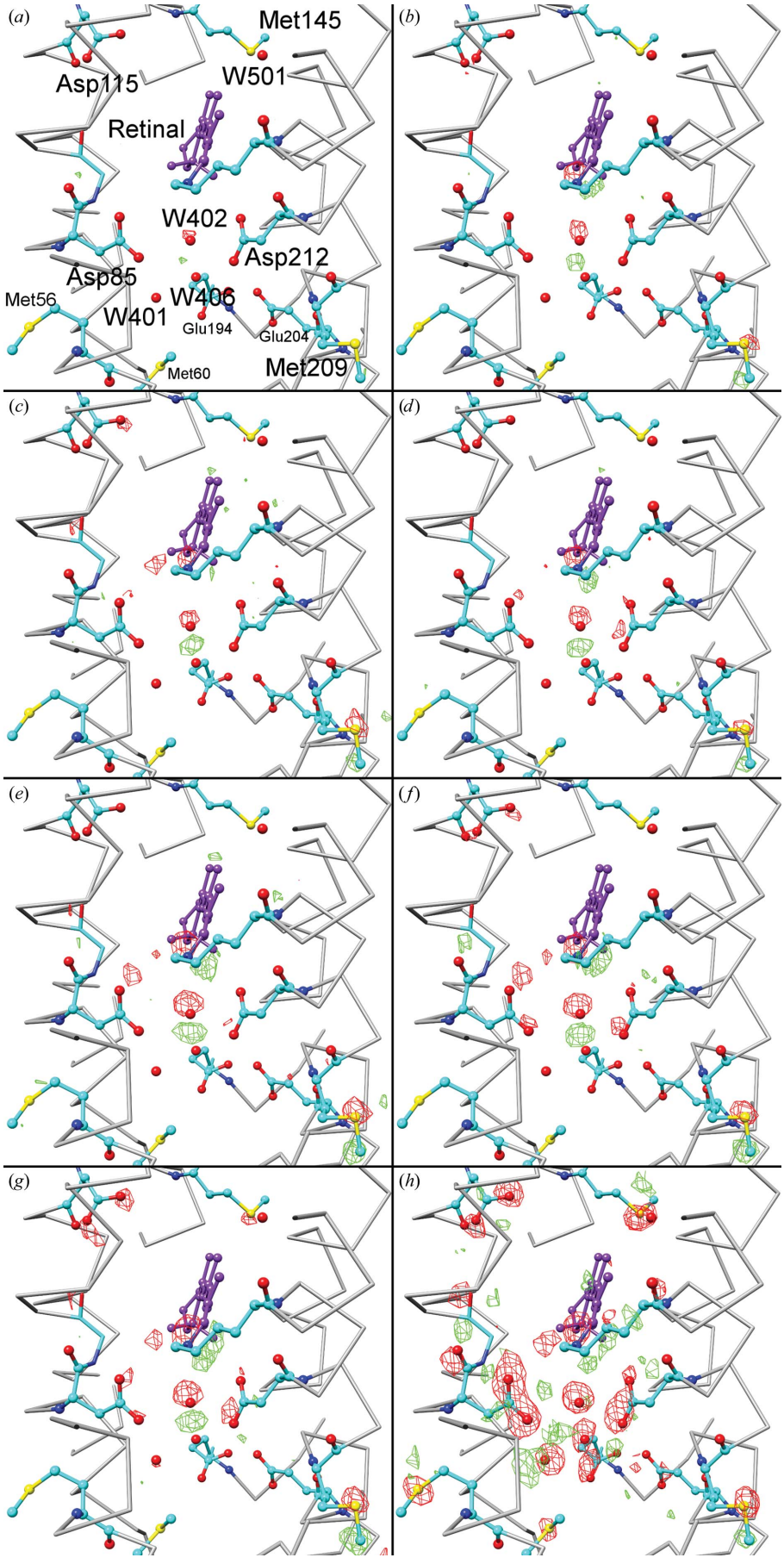

with i = 6, 7 and 8 are almost identical. Starting from the ($|F_4|$ − $|F_1|$) map, negative density also develops at the Asp85, Asp212 and Asp115 side chains. However, these densities are relatively small and do not increase monotonically with dose. The decarboxylation of the corresponding aspartic acid residues (which was widely observed as specific radiation damage of bR crystals; Borshchevskiy *et al.*, 2011) is low even after the collection of the eighth data set.

3.2. Specific radiation damage in the bacteriorhodopsin structure

The crystal accumulated about 1 MGy between the first and the ninth data set, as described in §2. Previously, specific radiation damage in the bR structure was detected at doses of >1.2 MGy (Borshchevskiy *et al.*, 2011). The ($|F_9|$ − $|F_1|$) difference map in Fig. 2(*h*) shows features of specific radiation damage in the bR active site similar to those previously described in Borshchevskiy *et al.* (2011). The main features observed are the decarboxylation of Asp85, Asp212, Asp115, Glu194 and Glu204, the disappearance of water molecules at the active site (W401, W402, W406 and W501), the change of conformations of the three methionine side chains (Met56, Met60 and Met145) and finally the appearance of the coupled positive/negative density peaks at the main-chain carboxyls of Lys216 and Asp85. Some of these features (the decarboxylation of Asp85 and, with increasing exposure time, of Glu194, Glu204 and Asp102) have been observed previously (Matsui *et al.*, 2002).

The absorbed dose accumulated between the first and the ninth data sets

Figure 2
Experimental difference Fourier electron-density maps ($|F_i|$ − $|F_1|$) at the active site of bR, where i = 2, 3, 4, 5, 6, 7, 8 and 9 are shown in (*a*), (*b*), (*c*), (*d*), (*e*), (*f*), (*g*) and (*h*), respectively. Negative (−5σ) and positive (5σ) densities are shown in red and green, respectively. The grey line traces the protein backbone; the side chains discussed in the text are shown in ball-and-stick representation. Retinal is shown in purple and is oriented perpendicular to the plane of the figure.

in the present study is close to that accumulated between the first and the fourth data sets in the previously published work (Borshchevskiy *et al.*, 2011). Therefore, one can assume that the difference maps shown in Fig. 2(*h*) (this study) and in Fig. 2(*b*) of Borshchevskiy *et al.* (2011) (subsequently referred to as Fig. $2b^{2011}$) should demonstrate the same structural changes. Indeed, all of the structural changes that were visible in the latter are reproduced in Fig. 2(*h*), although the corresponding peaks in the difference electron-density map are much higher in the present work. However, some details of bR radiation damage which are well distinguished in Fig. 2(*h*) were not observed by Borshchevskiy *et al.* (2011) and only became noticeable at larger absorbed doses (for instance in Fig. $2d^{2011}$). This feature probably relates to the quality of the experimental data and demonstrates the importance of using nontwinned crystals for the investigation of structural changes in protein molecules: the X-ray data resolution is almost identical in both studies but the twinning ratio in the previous work was as high as 38%, compared with 0% here.

It has previously been reported that specific radiation-damage effects in protein crystals at 100 K vary with different dose rates for the same total X-ray dose (Leiros *et al.*, 2006). Leiros and coworkers studied maltooligosyltrehalose trehalohydrolase and trypsin at tenfold and 24-fold dose-rate differences, respectively, and demonstrated that larger dose rates result in small measurable increases in damage at radiation-sensitive sites. A similar dose-rate effect seems to be unlikely to be responsible for the differences between the structures shown in Fig. 2(*h*) and Fig. $2b^{2011}$ since the experiments for both studies were performed on the same beamline with similar flux and beam attenuation.

It is important to emphasize two observations. (i) The difference densities at the Met209 side chain in the $(|F_9| - |F_1|)$ map are almost the same as in the $(|F_8| - |F_1|)$ map. This means that conformational changes of Met209 took place at low dose and remain the same during further irradiation. (ii) The positive density corresponding to a new position of W401 disappears in the $(|F_9| - |F_1|)$ map. Small absorbed doses result in a shift of W401 but larger doses cause its disappearance from the region. These two facts imply that there are two separate processes taking place during X-ray absorption by bR crystals. The first process occurs at low absorbed doses and reveals itself as displacements of the SB, W402 and Met209. These changes saturate after the absorption of ∼0.15 MGy as follows from the fact that the $(|F_i| - |F_1|)$ maps with $i = 6, 7$ and 8 are virtually identical. Therefore, the first process can be associated with the formation of the orange species. The second process takes place at higher doses and occurs as severe modifications of the active site as described in detail previously (Borshchevskiy *et al.*, 2011).

At an absorbed dose of ∼0.8 MGy almost no difference density was observed in Fig. $2a^{2011}$, while significant differences are observed in the present study in Fig. 2(*c*) (absorbed dose ∼0.12 MGy). The crystal absorbed ∼0.4 MGy during the first data-set collection in Borshchevskiy *et al.* (2011), which is far more than the saturation dose for formation of the orange species (∼0.15 MGy as follows from Figs. 2 and 5). Therefore, the amount of orange species is equal in all data sets in the previous study, and corresponding structural changes are not detected in the electron-density difference maps shown in Fig. 2^{2011}.

3.3. Structure of the orange species

As follows from Fig. 2, structural changes associated with the formation of the orange species can be detected in difference electron-density $(|F_i| - |F_1|)$ maps with $i = 2, \ldots, 8$. The F_8 data set and $(|F_8| - |F_1|)$ difference map (shown in Fig. 2*g*) were used to deduce a structural model for the orange species of bR. A comparison of the ground state and the orange species is shown in Fig. 3. The refinement statistics of the data used in model building for the ground state and the

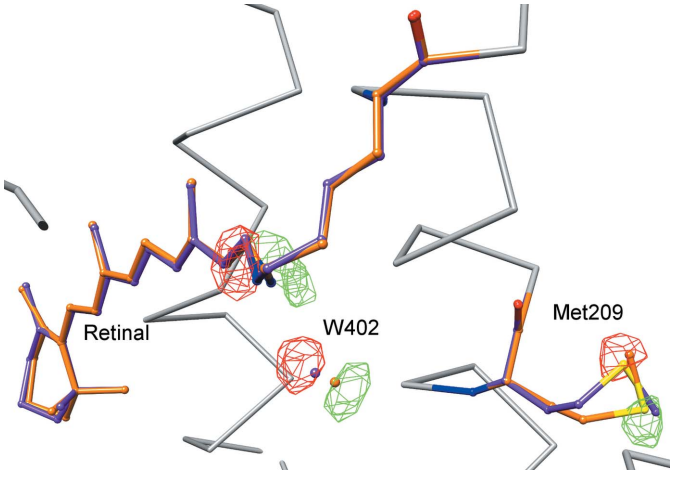

Figure 3
Comparison of the ground and orange states of bR. The molecular backbone is shown in grey. Water molecule W402, Met209 and retinal with Lys215 in the ground and orange states are shown in purple and orange, respectively. The negative and positive difference densities of the $(|F_8| - |F_1|)$ map are shown in red and green, respectively. The map is shown at 5σ.

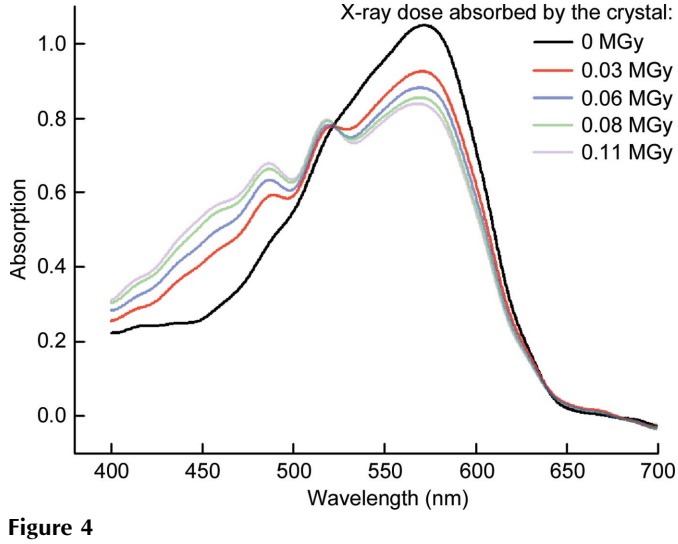

Figure 4
X-ray-induced absorption changes in the $P6_3$ bR crystal corresponding to the formation of the orange species.

orange species are shown in Table 1. In the orange species, the retinal remains attached to the Lys215 side chain and the SB is shifted by 0.4 Å, which corresponds to a rotation around C14—C15 by ∼15°. Simultaneously, W402 is moved by 0.6 Å and maintains a hydrogen bond to the SB, the length of which changes from 2.8 to 3.1 Å. The difference densities on Met209 refer to the conformational change with swapped S^D and C^E atoms.

3.4. Spectroscopic study of orange-species formation

To prove that the observed structural rearrangements do correspond to the formation of the orange species, changes in the UV–Vis absorption spectrum were monitored with an online microspectrophotometer (McGeehan *et al.*, 2009). Fig. 4 presents the spectroscopic changes of a bR crystal under X-ray illumination. The absorption peak corresponding to the ground state at 570 nm decays and new peaks arise at 485 and 516 nm. These spectroscopic changes are in agreement with those previously assigned to the formation of the orange species (Matsui *et al.*, 2002), although the positions of these peaks are slightly different from those reported in the previous study: 576 nm for the ground state and 478/510 nm for the orange species. This discrepancy could be owing to the different crystal packing and different buffers employed in the previous study (Matsui *et al.*, 2002) and the present study. In addition, one of the peaks (450 nm) reported previously (Matsui *et al.*, 2002) strongly overlaid with the emerging background from the buffer in our experiments and thus is not under discussion here.

The dependence of the orange-state occupancy on the dose absorbed by the crystal can be calculated separately from the structural and spectroscopic data as described in §2. These dependencies are compared in Fig. 5. As can be seen, the data from the two crystals used for the crystallographic studies coincide well and both conform to the spectroscopic data collected from a thinner crystal. The close coincidence of the structural and spectroscopic data confirms that the observed structural rearrangements correspond to the formation of the orange species.

4. Discussion

Radiation damage in macromolecular crystallography at cryogenic temperatures has so-called global and specific manifestations (Garman & Weik, 2013). Global radiation damage refers to the loss of diffraction quality of the crystals. It has been suggested (Meents *et al.*, 2010) that hydrogen gas formed inside the sample during irradiation is one of the major causes of global radiation damage.

In contrast, specific manifestations of radiation damage are caused by electron-gain centres which are formed as a product of the primary absorption of a photon. Each primary photoelectron has enough energy to subsequently produce up to ∼500 secondary electrons which are able to induce further ionization and gradually become thermalized. Thermalized electrons can be trapped by molecules, forming electron-gain centres. Electron tunnelling occurs along the protein backbone until the electron is trapped by electron-affinic sites in the protein (Jones *et al.*, 1987; Garman, 2010). Consequently, the specific effects describe chemical and structural changes, such as for example the reduction of disulfide bonds, the decarboxylation of acidic amino-acid residues, the reduction of metal centres and changes in the electronic structure of chromorphores. The latter can be conveniently monitored by online microspectroscopy (McGeehan *et al.*, 2009) and appear to already be significant at doses three orders of magnitude below the Garman limit of 30 MGy (Owen *et al.*, 2006) (tens of kGy in Denisov *et al.*, 2007; Meharenna *et al.*, 2010; Hersleth & Andersson, 2011; Owen *et al.*, 2011). In the present study, it has been shown that structural alterations, in addition to spectroscopic changes, can be detected in bR at such a low absorbed dose (500 times less than the Garman limit) without evidence of loss of crystal diffraction quality or covalent-bond breakage.

As follows from the spectroscopic data, the absorption peak of the orange species is blue-shifted in comparison to the native state. The structural data help possible origins of this shift to be understood. There are several issues that influence the opsin shift of the retinal (Lasogga *et al.*, 2010): (i) the electrostatic field induced by charged residues or dipolar groups within the protein (Hoffmann *et al.*, 2006; Fujimoto *et al.*, 2007), (ii) the geometry of the chromophore (Hoffmann *et al.*, 2006), (iii) the counterion near the SB nitrogen (Marti *et al.*, 1991, 1992; Hoffmann *et al.*, 2006; Sekharan *et al.*, 2007) and (iv) the hydrogen-bonding network at the active site (Hoffmann *et al.*, 2006; Fujimoto *et al.*, 2007; Sekharan *et al.*, 2007). There is no visible structural change related to charged residues or dipolar groups within the retinal-binding pocket.

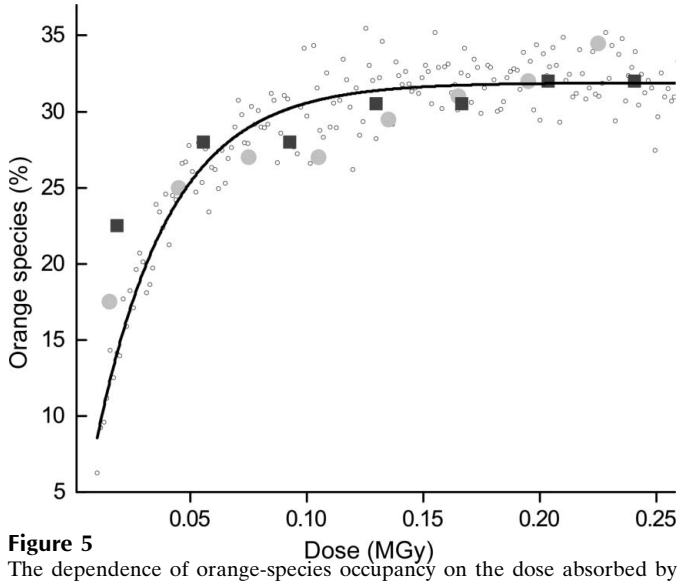

Figure 5
The dependence of orange-species occupancy on the dose absorbed by the crystal calculated from spectroscopic (small circles) and X-ray crystallographic data (big circles and squares for 1st and 2nd crystals, respectively). The fraction of bR in the orange species was estimated as the mean occupancies of W402, the N atom of the SB and the S^D atom of Met209. The increase in the fraction of the orange species is fitted by an exponent (shown as a black line) with an exponential constant of 33 MGy^{-1}. The fit is to the spectroscopic data.

The only structural change in the protein (besides SB and W402) is the conformation of Met209, which is more than 10 Å away from the retinal. Thus, mechanism (i) for a spectral shift is quite improbable. However, an influence of Met209 on the state of the retinal cannot be excluded since the changes of Met209, SB and W402 with absorbed dose are concomitant. One can speculate that the two conformations of Met209 may be related to the presence of several absorption peaks in the visible absorption spectrum corresponding to the formation of the orange species.

The retinal geometry is more planar in the orange species, which effectively elongates the conjugated π-electron system and thereby should shift the spectrum to the red. Since this conclusion is in contradiction with the current observations, mechanism (ii) plays a minor role in spectral changes.

The distance between the SB and the Asp85 side chain is almost the same in the two states; however, the SB approaches Asp212 in the structure of the orange species (the distance between SB and Asp212 O^{D1} changes from 4.0 Å in the ground state to 3.7 Å in the orange species), thus enhancing the interaction with the counterion. The SB–W402 conformation is more favourable for the hydrogen bond in the orange species. Therefore, mainly mechanisms (iii) and (iv) contribute to the blue shift since they stabilize the orange state. It seems probable that it is electrons produced by the primary photoelectrons and trapped by the active site which disturb the hydrogen-bond network and enhance the interaction with the counterion.

The orange species has a three-peaked absorption band which is characteristic of the retro form of retinal (Schreckenbach *et al.*, 1977; Matsui *et al.*, 2002). The three-peaked absorption band may also be related to a steric interaction of retinal and the protein or may result from the contribution of two or more species to the observed absorption band (Schreckenbach *et al.*, 1977). With the X-ray structure of the orange species now being available, theoretical calculations could give an exact answer as to the origin of the spectral blue shift and the three-peak absorption band associated with the orange species.

As follows from Fig. 5, for X-ray data collection from bR in the ground state about 30% of protein molecules convert to the orange species after the absorption of 0.15 MGy. The same amount of orange species was accumulated during data collection for the published crystallographic data of bR in the ground state (Pebay-Peyroula *et al.*, 1997; Luecke *et al.*, 1998, 1999; Belrhali *et al.*, 1999; Edman *et al.*, 1999; Facciotti *et al.*, 2001; Matsui *et al.*, 2002; Schobert *et al.*, 2002; Lanyi & Schobert, 2007). However, no structural evidence for the presence of the orange species has previously been reported. Since the structural changes associated with the formation of the orange species are small, a direct comparison of high-resolution X-ray data from crystals with significantly different contents of the orange species was necessary to identify them. The presence of the orange species could manifest itself as alternative conformations of retinal SB, W402 and Met209 in previously published structures of the bR ground state. In our model, six residues (Arg7, Leu15, Leu48, Ser132, Ser183, Asn202) have alternative conformations. However, the two 'best' crystallographic models of the bR ground state [PDB entries 1c3w at 1.55 Å resolution (Luecke *et al.*, 1999) and 1qhj at 1.9 Å resolution (Belrhali *et al.*, 1999)] provide no alternative conformation for these residues or for the SB, W402 and Met209. This probably means that the quality of the previously available data was not sufficient to observe any alternate conformations. In addition, the 1c3w and 1qhj data were collected with a significantly higher X-ray dose. This implies that the previously published data for the bR ground state have a certain non-negligible contribution from the protein after radiolysis which has modified the active site (as shown in Borshchevskiy *et al.*, 2011). It may complicate the interpretation of electron densities at the active site and the identification of structural changes accompanying the formation of the orange species.

The present study is a necessary step on the way towards understanding the bR proton-pumping mechanism. The structural information on the orange species should be taken into account when interpreting the X-ray data from bR crystals, especially for high-resolution studies. We believe that the results of the present work extend beyond the problem of the formation of bR orange species. Our observation that an absorbed dose about three orders of magnitude below the 30 MGy limit significantly changes the bR structure may also be relevant for crystals of other proteins. Further studies with other proteins could give more details of structural alterations under the absorption of low X-ray doses and future experiments with femtosecond X-ray pulses from free-electron lasers might open alternative ways to circumvent the problem of radiation-induced structural changes (Lomb *et al.*, 2011; Bogan, 2013).

We are grateful to the ESRF for the allocation of beam time and to Antoine Royant and Philippe Carpentier for their help regarding the online spectroscopic experiments. We acknowledge Eva Pebay-Peyroula for support of this work and for reading the manuscript. We are grateful to the Structural Biology Group of ESRF for allocated beamtime and particularly to Alexandr Popov for valuable comments and discussions. We are very grateful to Professor Elspeth Garman and to the anonymous referees for their numerous suggestions and extensive editing, which enormously improved the manuscript. This work was supported by the CEA(IBS)–HGF(FZJ) STC 5.1 specific agreement. Part of this work was supported by the German Federal Ministry for Education and Research (PhoNa; Photonic Nanomaterials). Protein expression, data treatment and manuscript preparation were supported by the Russian Scientific Foundation (No. 14-14-00995).

References

Adams, P. D. *et al.* (2010). *Acta Cryst.* D**66**, 213–221.
Balashov, S. P. & Ebrey, T. G. (2001). *Photochem. Photobiol.* **73**, 453–462.
Belrhali, H., Nollert, P., Royant, A., Menzel, C., Rosenbusch, J. P., Landau, E. M. & Pebay-Peyroula, E. (1999). *Structure*, **7**, 909–917.
Bogan, M. J. (2013). *Anal. Chem.* **85**, 3464–3471.

Borshchevskiy, V., Efremov, R., Moiseeva, E., Büldt, G. & Gordeliy, V. (2010). *Acta Cryst.* D**66**, 26–32.
Borshchevskiy, V. I., Round, E. S., Popov, A. N., Büldt, G. & Gordeliy, V. I. (2011). *J. Mol. Biol.* **409**, 813–825.
Bourgeois, D. (1999). *Acta Cryst.* D**55**, 1733–1741.
Bourenkov, G. P. & Popov, A. N. (2006). *Acta Cryst.* D**62**, 58–64.
Brünger, A. T., Adams, P. D., Clore, G. M., DeLano, W. L., Gros, P., Grosse-Kunstleve, R. W., Jiang, J. S., Kuszewski, J., Nilges, M., Pannu, N. S., Read, R. J., Rice, L. M., Simonson, T. & Warren, G L (1998). *Acta Cryst.* D**54**, 905–921.
Denisov, I. G., Victoria, D. C. & Sligar, S. G. (2007). *Radiat. Phys. Chem.* **76**, 714–721.
Edman, K., Nollert, P., Royant, A., Belrhali, H., Pebay-Peyroula, E., Hajdu, J., Neutze, R. & Landau, E. M. (1999). *Nature (London)*, **401**, 822–826.
Emsley, P. & Cowtan, K. (2004). *Acta Cryst.* D**60**, 2126–2132.
Evans, P. (2006). *Acta Cryst.* D**62**, 72–82.
Facciotti, M. T., Rouhani, S., Burkard, F. T., Betancourt, F. M., Downing, K. H., Rose, R. B., McDermott, G. & Glaeser, R. M. (2001). *Biophys. J.* **81**, 3442–3455.
Freier, E., Wolf, S. & Gerwert, K. (2011). *Proc. Natl Acad. Sci. USA*, **108**, 11435–11439.
Fujimoto, K., Hayashi, S., Hasegawa, J. & Nakatsuji, H. (2007). *J. Chem. Theory Comput.* **3**, 605–618.
Garman, E. (1999). *Acta Cryst.* D**55**, 1641–1653.
Garman, E. F. (2010). *Acta Cryst.* D**66**, 339–351.
Garman, E. F. & Weik, M. (2013). *J. Synchrotron Rad.* **20**, 1–6.
Gonzalez, A. & Nave, C. (1994). *Acta Cryst.* D**50**, 874–877.
Gordeliy, V. I., Schlesinger, R., Efremov, R., Büldt, G. & Heberle, J. (2003). *Methods Mol. Biol.* **228**, 305–316.
Heberle, J. (2000). *Biochim. Biophys. Acta*, **1458**, 135–147.
Henderson, R. (1990). *Proc. R. Soc. B Biol. Sci.* **241**, 6–8.
Hersleth, H. P. & Andersson, K. K. (2011). *Biochim. Biophys. Acta*, **1814**, 785–796.
Hirai, T., Subramaniam, S. & Lanyi, J. K. (2009). *Curr. Opin. Struct. Biol.* **19**, 433–439.
Hoffmann, M., Wanko, M., Strodel, P., König, P. H., Frauenheim, T., Schulten, K., Thiel, W., Tajkhorshid, E. & Elstner, M. (2006). *J. Am. Chem. Soc.* **128**, 10808–10818.
Holton, J. M. (2009). *J. Synchrotron Rad.* **16**, 133–142.
Jones, G. D., Lea, J. S., Symons, M. C. & Taiwo, F. A. (1987). *Nature (London)*, **330**, 772–773.
Kmetko, J., Husseini, N. S., Naides, M., Kalinin, Y. & Thorne, R. E. (2006). *Acta Cryst.* D**62**, 1030–1038.
Lanyi, J. K. (2004*a*). *Annu. Rev. Physiol.* **66**, 665–688.
Lanyi, J. K. (2004*b*). *Biochim. Biophys. Acta*, **1658**, 14–22.
Lanyi, J. K. & Schobert, B. (2007). *J. Mol. Biol.* **365**, 1379–1392.
Lasogga, L., Rettig, W., Otto, H., Wallat, I. & Bricks, J. (2010). *J. Phys. Chem. A*, **114**, 2179–2188.
Leiros, H.-K. S., Timmins, J., Ravelli, R. B. G. & McSweeney, S. M. (2006). *Acta Cryst.* D**62**, 125–132.
Leslie, A. G. W. & Powell, H. R. (2007). *Evolving Methods for Macromolecular Crystallography*, edited by R. J. Read & J. L. Sussman, pp. 41–51. Dordrecht: Springer.
Lomb, L. *et al.* (2011). *Phys. Rev. B*, **84**, 214111.
Luecke, H., Richter, H. T. & Lanyi, J. K. (1998). *Science*, **280**, 1934–1937.
Luecke, H., Schobert, B., Richter, H.-T., Cartailler, J.-P. & Lanyi, J. K. (1999). *J. Mol. Biol.* **291**, 899–911.
Marti, T., Otto, H., Rösselet, S. J., Heyn, M. P. & Khorana, H. G. (1992). *J. Biol. Chem.* **267**, 16922–16927.
Marti, T., Rösselet, S. J., Otto, H., Heyn, M. P. & Khorana, H. G. (1991). *J. Biol. Chem.* **266**, 18674–18683.
Matsui, Y., Sakai, K., Murakami, M., Shiro, Y., Adachi, S., Okumura, H. & Kouyama, T. (2002). *J. Mol. Biol.* **324**, 469–481.
McGeehan, J., Ravelli, R. B. G., Murray, J. W., Owen, R. L., Cipriani, F., McSweeney, S., Weik, M. & Garman, E. F. (2009). *J. Synchrotron Rad.* **16**, 163–172.
Meents, A., Gutmann, S., Wagner, A. & Schulze-Briese, C. (2010). *Proc. Natl Acad. Sci. USA*, **107**, 1094–1099.
Meharenna, Y. T., Doukov, T., Li, H., Soltis, S. M. & Poulos, T. L. (2010). *Biochemistry*, **49**, 2984–2986.
Metzler, D. E. & Harris, C. M. (1978). *Vision Res.* **18**, 1417–1420.
Murray, J. W., Rudiño-Piñera, E., Owen, R. L., Grininger, M., Ravelli, R. B. G. & Garman, E. F. (2005). *J. Synchrotron Rad.* **12**, 268–275.
Murshudov, G. N., Skubák, P., Lebedev, A. A., Pannu, N. S., Steiner, R. A., Nicholls, R. A., Winn, M. D., Long, F. & Vagin, A. A. (2011). *Acta Cryst.* D**67**, 355–367.
Owen, R. L., Rudiño-Piñera, E. & Garman, E. F. (2006). *Proc. Natl Acad. Sci. USA*, **103**, 4912–4917.
Owen, R. L., Yorke, B. A., Gowdy, J. A. & Pearson, A. R. (2011). *J. Synchrotron Rad.* **18**, 367–373.
Pebay-Peyroula, E., Rummel, G., Rosenbusch, J. P. & Landau, E. M. (1997). *Science*, **277**, 1676–1681.
Perrakis, A., Morris, R. & Lamzin, V. S. (1999). *Nature Struct. Biol.* **6**, 458–463.
Pettersen, E. F., Goddard, T. D., Huang, C. C., Couch, G. S., Greenblatt, D. M., Meng, E. C. & Ferrin, T. E. (2004). *J. Comput. Chem.* **25**, 1605–1612.
Schobert, B., Cupp-Vickery, J., Hornak, V., Smith, S. & Lanyi, J. (2002). *J. Mol. Biol.* **321**, 715–726.
Schreckenbach, T., Walckhoff, B. & Oesterhelt, D. (1977). *Eur. J. Biochem.* **76**, 499–511.
Sekharan, S., Sugihara, M. & Buss, V. (2007). *Angew. Chem. Int. Ed. Engl.* **46**, 269–271.
Takeda, K., Matsui, Y., Kamiya, N., Adachi, S., Okumura, H. & Kouyama, T. (2004). *J. Mol. Biol.* **341**, 1023–1037.
Wickstrand, C., Dods, R., Royant, A. & Neutze, R. (2014). *Biochim. Biophys. Acta*, doi:10.1016/j.bbagen.2014.05.021.
Winn, M. D. *et al.* (2011). *Acta Cryst.* D**67**, 235–242.
Yamamoto, M., Hayakawa, N., Murakami, M. & Kouyama, T. (2009). *J. Mol. Biol.* **393**, 559–573.
Yeates, T. O. (1997). *Methods Enzymol.* **276**, 344–358.
Zeldin, O. B., Gerstel, M. & Garman, E. F. (2013). *J. Appl. Cryst.* **46**, 1225–1230.